RSC Advances

PAPER

Cite this: *RSC Adv.*, 2022, **12**, 30892

Sonoelectrochemical oxidation of sulfamethoxazole in simulated and actual wastewater on a piezo-polarizable FTO/$BaZr_xTi_{(1-x)}O_3$ electrode: reaction kinetics, mechanism and reaction pathway studies†

Babatope O. Ojo,[a] Omotayo A. Arotiba [ab] and Nonhlangabezo Mabuba [*ab]

The sonoelectrochemical (SEC) oxidation of sulfamethoxazole (SMX) in simulated and actual wastewater on FTO/$BaZr_{(0.1)}Ti_{(0.9)}O_3$, FTO/$BaZr_{(0.05)}Ti_{(0.95)}O_3$ and FTO/$BaTiO_3$ electrodes is hereby presented. Electrodes from piezo-polarizable $BaZr_{(0.1)}Ti_{(0.9)}O_3$, $BaZr_{(0.05)}Ti_{(0.95)}O_3$, and $BaTiO_3$ materials were prepared by immobilizing these materials on fluorine-doped tin dioxide (FTO) glass. Electrochemical characterization performed on the electrodes using chronoamperometry and electrochemical impedance spectroscopy techniques revealed that the FTO/$BaZr_{(0.1)}Ti_{(0.9)}O_3$ anode displayed the highest sonocurrent density response of 2.33 mA cm^{-2} and the lowest charge transfer resistance of 57 Ω. Compared to other electrodes, these responses signaled a superior mass transfer on the FTO/$BaZr_{(0.1)}Ti_{(0.9)}O_3$ anode occasioned by an acoustic streaming effect. Moreover, a degradation efficiency of 86.16% (in simulated wastewater), and total organic carbon (TOC) removal efficiency of 63.16% (in simulated wastewater) and 41.47% (in actual wastewater) were obtained upon applying the FTO/$BaZr_{(0.1)}Ti_{(0.9)}O_3$ electrode for SEC oxidation of SMX. The piezo-polarizable impact of the FTO/$BaZr_{(0.1)}Ti_{(0.9)}O_3$ electrode was further established by the higher rate constant obtained for the FTO/$BaZr_{(0.1)}Ti_{(0.9)}O_3$ electrode as compared to the other electrodes during SEC oxidation of SMX under optimum operational conditions. The piezo-potential effect displayed by the FTO/$BaZr_{(0.1)}Ti_{(0.9)}O_3$ electrode can be said to have impacted the generation of reactive species, with hydroxyl radicals playing a predominant role in the degradation of SMX in the SEC system. Additionally, a positive synergistic index obtained for the electrode revealed that the piezo-polarization effect of the FTO/$BaZr_{(0.1)}Ti_{(0.9)}O_3$ electrode activated during sonocatalysis combined with the electrochemical oxidation process during SEC oxidation can be advantageous for the decomposition of pharmaceuticals and other organic pollutants in water.

Received 5th August 2022
Accepted 13th October 2022

DOI: 10.1039/d2ra04876k

rsc.li/rsc-advances

1 Introduction

Consumption of and demand for pharmaceutical compounds towards the improvement of human and animal health have increased tremendously in the last few decades. This occurrence can be attributed to an unprecedented surge in world population and increased dependency on these substances for health improvement. Unfortunately, these pharmaceuticals have become emerging contaminants in the environment and their pollution effect is a subject that has attracted increased scrutiny in recent times. The extensive use of pharmaceuticals for human health and unregulated methods of disposal are contributing factors to their persistent presence in the environment.[1–3] Pharmaceuticals have been reported to be present and detected within the concentration range of ng L^{-1} to μg L^{-1} in soils, surface water, groundwater, and wastewater treatment plants.[4,5] Classes of pharmaceuticals that are commonly detected in water include antibiotics, analgesics, antiviral among others. Sulfamethoxazole (SMX), a commonly prescribed antibiotic for the prevention and treatment of various infectious bacterial diseases in human and animal, has been reportedly found in various water bodies.[2,6,7] Concerns have been heightened over possible adverse effects of antibiotics present in the environment. For instance, the formation of antibiotics resistive microorganisms arising from increased presence of these antibiotics in the environment is a potential risk to both aquatic lives and public health.[8,9] These microorganisms can lessen the therapeutic activity of antibiotics against infectious diseases in human and animal pathogens.[10] Though several analytical techniques have been successfully

[a]*Department of Chemical Sciences, University of Johannesburg, Doornfontein 2028, Johannesburg, South Africa. E-mail: nmabuba@uj.ac.za*

[b]*Centre for Nanomaterials Science Research, University of Johannesburg, South Africa*

† Electronic supplementary information (ESI) available. See DOI: https://doi.org/10.1039/d2ra04876k

utilized for the identification and quantification of pharmaceuticals in low concentration levels, conventional method commonly employed for their removal have not been completely efficient.[10–12] For instance, several pharmaceuticals have reportedly been detected in the influent and effluents of conventional wastewater treatment plants.[5,13]

Several analytical methods categorized as advanced oxidation processes (AOP) have found increasing application toward the removal of pharmaceuticals in water.[14–19] These processes make use of highly reactive species generated during these processes to perform the non-selective decomposition of various organic pollutants in water.[20,21] Among these methods, sonoelectrochemical (SEC) oxidation technique has been proven to be a potent method for the decomposition organic waste present in water than other conventional techniques.[22] Typically, the positive synergistic mechanism possessed by SEC, which arises from combining the ultrasonic wave effects with electrochemical oxidation process, can help achieve complete removal of these recalcitrant pollutants in water.[23] Furthermore, SEC technique presents advantages such as micro mixing, microjet and shockwave formation, elimination of electrode passivation through acoustic streaming and acoustic cavitation during the process. These advantages contribute to the efficiency of SEC process by improving the reaction rate, hastening mass transfer of analyte across the solution–analyte interface to the electrode, and perpetual cleaning of the electrode surface through degassing action caused by the implosion of bubble cavitation.[22–24] Several electrode materials such as boron doped diamond (BDD),[25–28] (lead dioxide) Ti/PbO_2,[29] Ti/Ta_2O_5–SnO_2,[30] Ti/RuO_2,[31,32] diamond coated niobium,[33] stainless steel[34] have been reported for SEC degradation of various organics in aqueous medium. However, piezoelectric materials which can generate highly reactive species such as hydroxyl and superoxide radicals in aqueous medium when agitated mechanically are not commonly explored for SEC applications.[35] These piezoelectric materials are materials that possess internal polarizable properties when exposed to mechanical stress. They have been known to possess high dielectric constant[36,37] which measures the ability of the material to be polarized by the application of an externally imposed force or field. This strain-induced polarization causes the development of non-zero dipole moment in the crystal lattice of the material, which subsequently results in the formation of charge potential localized at the opposite surface of the material.[38] These charges interact with hydroxyl ion and oxygen to produce hydroxyl and superoxide radicals respectively[39] for the degradation of organic pollutants. Piezoelectric materials have also been widely applied for energy harvesting.[40–42] However, their piezo potential for environmental applications such as water treatment is only beginning to unfold. Commonly applied piezocatalytic materials for water treatment purposes include $BaZrO_3$, $BaTiO_3$ $CaTiO_3$, $BiWO_6$, MoS_2, $PbZrTiO_3$, $KNbO_3$ $BaZr_xTi_{(1-x)}O_3$.[43–48] However, little is known about their applications for ultrasound enhanced electrochemical oxidation or SEC degradation of organic pollutants in water. Even though barium titanate ($BaTiO_3$) is a prominent piezoelectric material for its high dielectric constant, it has been reported that incorporating Zr into the crystal structure of $BaTiO_3$ can improve its piezoelectric property.[49–51] Whereas $BaTiO_3$ has been employed for the degradation of ciprofloxacin polluted wastewater using SEC oxidation technique,[52] barium zirconate titanate (BZT) is environmentally friendly and thermally stable piezoelectric material.[53] Since it has not been reported for the decomposition of pharmaceutical contaminated wastewater, it contributes to the novelty of this manuscript.

Hence, this work present for the first time, the SEC oxidation of sulfamethoxazole (SMX) in simulated and actual wastewater using FTO/$BaZr_xTi_{(1-x)}O_3$ (x = 0, 0.05 and 0.1) electrodes. Moreover, the influence of ultrasound towards the activation of the electrode surface and property during SEC process are enumerated, while the positive synergy of combining the piezopotential of the $BaZr_xTi_{(1-x)}O_3$ material with SEC oxidation during the treatment of SMX in water is also highlighted in this work. The SEC system set-up and the application of the fabricated piezoelectric electrodes for sonocatalysis, electrochemical oxidation and a combination of both methods (SEC oxidation) for the decomposition of SMX in simulated and actual wastewater were investigated and reported. Finally, the reaction mechanism and reaction pathway suggesting the possible route through which the reactive radicals responsible for the decomposition of the pollutant in the system were generated and the byproduct of the decomposed SMX were also investigated.

2. Materials and methods

2.1. Chemicals

The chemical reagents employed for this study were ordered from Sigma Aldrich (South Africa) and were used as received. Barium acetate ($Ba(CH_3COO)_2$), titanium(IV) butoxide ($(C_4H_9O)_4Ti$) and zirconium dioxide (ZrO_2) were used as precursors for the BZT synthesis while *N*-methyl-2-pyrrolidone (NMP) and polyvinylidene fluoride (PVDF) were employed as the binding agent for coating the $BaTiO_3$ and $BaZr_xTi_{(1-x)}O_3$ powders on the substrate. Fluorine doped tin dioxide (FTO) glass (5 cm × 15 cm × 3 cm, surface resistivity of ~8 Ω sq^{-1}) was employed as substrate for the synthesized materials. The fabricated FTO/$BaZr_xTi_{(1-x)}O_3$ and FTO/$BaTiO_3$ electrodes were used as the working electrode while platinum wire and Ag/AgCl were employed as counter and reference electrode, respectively.

2.2. Synthesis of $BaTiO_3$

$BaTiO_3$ particle was synthesized using a sol–gel approach earlier reported by Ojo *et al.*[52] Briefly, 0.02 mol ($Ba(CH_3COO)_2$) was dissolved in a mixture of acetic acid and ethylene glycol and stirred for 15 min in a beaker, followed by the addition of 0.034 mol ($(C_4H_9O)_4Ti$) and acetyl acetone. This mixture was then stirred for an hour at ambient temperature. The resulting $BaTiO_3$ sol–gel was heated in the oven for 1 h at 120 °C and then calcined in a muffle furnace at 900 °C for 3 h. The obtained $BaTiO_3$ was left to cool and finally crushed into fine powder.

2.3. Synthesis of $BaZr_xTi_{(1-x)}O_3$ ($x = 0.05$ and 0.1)

Similar synthetic method employed in the preparation of $BaTiO_3$ were used in the synthesis of $BaZr_{(0.1)}Ti_{(0.9)}O_3$ and $BaZr_{(0.05)}Ti_{(0.95)}O_3$ particles with the addition of an appropriate amount of ZrO_2. Firstly, 2 : 1 molar ratio or 0.005 mol : 0.0025 mol of (ZrO_2) were respectively added to different beakers each containing 0.02 mol of ($Ba(CH_3COO)_2$). The dissolution of this mixture was performed by adding acetic acid and ethylene glycol to the beaker and stirred for 30 min. This was accompanied by the inclusion of 0.032 mol and 0.029 mol of ($(C_4H_9O)_4Ti$) and acetyl acetone to the respective beakers designated for $BaZr_{(0.1)}Ti_{(0.9)}O_3$ and $BaZr_{(0.05)}Ti_{(0.95)}O_3$, respectively. The subsequent mixture was allowed to stir for 1 h at ambient temperature and later subjected to heat in the oven for 2 h at 100 °C. Finally, the particles were annealed in a muffle furnace at 900 °C for 2 h to obtain $BaZr_{(0.1)}Ti_{(0.9)}O_3$ and $BaZr_{(0.05)}Ti_{(0.95)}O_3$ particles. The particles were then left to cool then crushed into fine powder.

2.4. Structural and morphological characterization of the piezoelectric materials

The purity and measure of crystallinity of the synthesized piezoelectric materials were investigated with Ultima IV X-ray diffractometer (Rigaku, Japan), which uses Cu Kα radiation ($k = 0.15406$), attached to K-beta filter at 30 mA and 40 kV. The morphological features of the materials were determined with transmission electron microscopy (TEM) (Joel JEM-2100, Japan) and field emission scanning electron microscope (FE-SEM) (Zeiss 540 ultra, Germany). The elemental composition of the material was obtained from energy-dispersive X-ray spectrometer (EDS) coupled with the FE-SEM.

2.5 Fabrication and electrochemical characterization of $FTO/BaTiO_3$ and $FTO/BaZr_xTi_{(1-x)}O_3$ electrodes

$FTO/BaTiO_3$ and $FTO/BaZr_{(0.1)}Ti_{(0.9)}O_3$ and $FTO/BaZr_{(0.05)}Ti_{(0.95)}O_3$ electrodes were fabricated by drop drying the particles on the FTO substrate. Briefly, FTO glass was subjected to pre-treatment by sonication in acetone and ultra-pure water for 15 min and dried at 60 °C in an oven. Prior to coating the particles on the FTO glass, 95 mg of each particle was dispersed into a mixture of 100 wt% NMP and 5 mg PVDF and allow to stir vigorously, to obtain an evenly mixed slurry of each particle. The resulting slurry of each particle was subsequently dropped meticulously on the conductive face of the pre-treated FTO glass to obtain a uniformly dispersed film of the particle on the substrate. The prepared electrode was left to dry in an oven at 60 °C for 2 h. This technique was also applied in the preparation of $FTO/BaZr_{(0.1)}Ti_{(0.9)}O_3$ and $FTO/BaZr_{(0.05)}Ti_{(0.95)}O_3$ and $FTO/BaTiO_3$ electrodes.

Cyclic voltammetry and electrochemical impedance spectroscopy of the fabricated electrodes were conducted inside an unpartitioned cylindrical electrochemical reactor containing 5 mM ferricyanide in 0.1 M KCl solution, while chronoamperometry was conducted in 0.1 M Na_2SO_4 electrolyte solution containing 5 mg L^{-1} of SMX. A three electrode pocketSTAT2 potentiostat (Ivium, Netherlands) system was employed for all electrochemical characterization and degradation experiments. Furthermore, the fabricated electrodes with an estimated geometrical area of 3.60 cm^{-2} were used as the working electrode, while Ag/AgCl and platinum wire were both employed as reference and counter electrodes, respectively.

2.6 Sonoelectrochemical, sonolysis and electrochemical oxidation setup

Sonoelectrochemical degradation of 5 mg L^{-1} SMX simulated wastewater and actual wastewater spiked with 5 mg L^{-1} SMX were also performed in the electrochemical cell with UP400St ultrasonic processor [Hielscher, Germany (24 KHz, 7 mm diameter probe head)] introduced as the source of ultrasound wave into the system. Sonocatalysis of the same concentration of SMX was performed in the two wastewater samples. A 40 W ultrasound power was applied for all experiments involving sonocatalysis and SEC oxidation of SMX while keeping the electrode at 15 mm distance from the ultrasound probe. The reactor containing the bulk solution was placed in a circulating water bath and a thermostat was connected to the system to ensure that the temperature in the bulk solution is kept at 30 ± 2 °C. Moreover, 2 V bias potential was applied to the system, while 0.1 M Na_2SO_4 was added to the bulk solution as the supporting electrolyte during SEC oxidation.

For electrochemical oxidation of SMX, the reactor which contains 5 mg L^{-1} of SMX and 0.1 M Na_2SO_4 as the supporting electrolyte was placed on a magnetic stirrer. The bulk solution was gently stirred while 2 V bias potential was applied to the system during the process. Moreover, the prepared electrodes were also applied as the working electrode, while Ag/AgCl and platinum wire were employed as reference and counter electrodes, respectively for both SEC and electrochemical oxidation processes. For all experiments, a total of 80 ml of the bulk solution was placed in the reactor for each process for a period of 120 min while maintaining the operating conditions for each process. Aliquots were taken from the bulk solution during each process every 20 min and analyzed to monitor the trend of concentration degradation and total organic carbon removal. The stability of the $FTO/BaZr_{(0.1)}Ti_{(0.9)}O_3$ electrode was investigated by subjecting the electrode to SEC oxidation of SMX in synthetic wastewater through five cycles, with a duration of 120 min per cycle. After each cycle, the electrode was rinsed with ultrapure water and dried in the oven at 60 °C for 15 min.

2.7 Degradation and total organic carbon analysis

Analysis to determine the efficiency of degradation of SMX at regular time intervals was investigated using ultraviolet (UV)-visible spectrophotometer. Analysis to determine the efficiency of TOC removed during each process was also carried out with Lotix QC03 TOC analyzer (Teledyne Tekmar, USA). The efficiency of each degradation process and the TOC removal efficiency of SMX in the bulk solution were estimated and obtained with the formula in presented in eqn (1) and (2).

$$\text{Degradation efficiency } (\%) = \frac{C_0 - C_t}{C_0} \times 100\% \quad (1)$$

$$\text{TOC removal efficiency } (\%) = \frac{\text{TOC}_0 - \text{TOC}_t}{\text{TOC}_0} \times 100\% \quad (2)$$

where C_0, C_t, TOC_0 and TOC_t represent the initial concentration, concentration at a particular time, initial total organic carbon and the total organic carbon at a particular time, respectively.

2.8 Ultra-performance liquid chromatography tandem mass spectrometer analysis

Analysis of the wastewater containing SMX after SEC degradation was performed using ultra-performance liquid chromatography-tandem to SYNAPT G1 mass spectrometer (UPLC-MS, Waters, USA). The chromatographic separation was carried out in a Waters HSS T3 C18 analytical column (150 mm × 2.1 mm, 1.8 μm) at an optimized column temperature of 60 °C, 10 μL injection volume and 10 min analysis time. The separation process was carried out using ultra-pure water with 10 mM formic acid (eluent A) and acetonitrile (eluent B). The elution procedure involves 98% eluent A at a flow rate of 0.4 mL min^{-1} maintained for 1 min, accompanied by a linear gradient to 2% eluent A at 6 min. These conditions were held for 1.5 min before changing to the initial conditions. The SYNAPT G1 mass spectrometer was performed under multiple reaction monitoring modes with positive and negative electrospray ionization, to aid the detection of phenolic and other ESI-compatible compounds. 2.5 KV capillary voltage and 0.1 s scan time covering 50–1200 Dalton mass range were used, while the source temperature and desolvation temperature were set at 120 °C and 450 °C respectively. Argon was used as collision gas while nitrogen was used as desolvation and nebulizer gas. Target compounds were identified based on matching chromatography retention time. Instrumental control, data acquisition and processing were performed using MassLynx V4.1 (Waters, USA).[52]

3 Results and discussions

3.1 Structural, elemental and morphological characteristics of the piezoelectric materials

The X-ray diffractograms of the piezoelectric materials ($BaTiO_3$, $BaZr_{(0.05)}Ti_{(0.95)}O_3$ and $BaZr_{(0.1)}Ti_{(0.9)}O_3$) are presented in Fig. 1a. In the diffraction pattern, major peaks observed for $BaTiO_3$ corresponds to the tetragonal phase of $BaTiO_3$ (JCPDS card no. 04-008-4641). This is corroborated by the uneven splitting observed at $2\theta \approx 45°$.[54,55] Additionally, it was observed that the diffraction peaks obtained for $BaZr_{(0.05)}Ti_{(0.95)}O_3$ and $BaZr_{(0.1)}Ti_{(0.9)}O_3$ also correspond to its tetragonal crystal phase as confirmed by JCPDS card no. 04-013-9936. No significant change was observed in the structure of $BaTiO_3$ and $BaZr_xTi_{(1-x)}O_3$ particles. However, the superior intensity observed for the peaks obtained for $BaZr_xTi_{(1-x)}O_3$ may be attributed to narrowed particle size distribution, which may arise as the composition of Zr increases from 0.05 to 0.1 in the crystal structure of $BaZr_xTi_{(1-x)}O_3$.[56] Moreover, the inclusion of Zr ion in the crystal lattices of the material did not have tangible effect on the centrosymmetric nature of the $BaZr_xTi_{(1-x)}O_3$ from the $BaTiO_3$ phase as the Zr ion fitted well in the sublattice Ti-site of the $BaZr_xTi_{(1-x)}O_3$ phase structure.[57] However, a slight shift to the left in the 2θ position of $BaZr_xTi_{(1-x)}O_3$ from that observed for $BaTiO_3$ can be attributed to the large radius of Zr^{4+} (0.720 Å) compared to a smaller radius of Ti^{4+} (0.605 Å).[48,57] The purity of the material was established by the absence of peaks corresponding to other phases of the materials. The elemental constituent obtained from the EDS spectrum of $BaZr_{(0.1)}Ti_{(0.9)}O_3$ and $BaTiO_3$ are presented in Fig. 1b and c, respectively. The existence of only Ba, Zr, Ti and O as the elemental components of the $BaZr_{(0.1)}Ti_{(0.9)}O_3$ further validates the purity of the synthesized piezoelectric material.

The FESEM images of the piezoelectric materials are presented in Fig. 1. The morphology of $BaTiO_3$ (Fig. 1d) shows the presence of stacked particles with irregular structures. However, with increased composition of Zr incorporated into the crystal structure of the $BaZr_{(x)}Ti_{(1-x)}O_3$ material, the boundaries of the particles became more prominent as observed in $BaZr_{(0.05)}Ti_{(0.95)}O_3$ (Fig. 1e) and $BaZr_{(0.1)}Ti_{(0.9)}O_3$ (Fig. 1f). Moreover, the arrangement of the particles appears to be more regular and the globular-like pattern of even shape became pronounced as the composition of Zr increased in BZT. Furthermore, growth of the grain size and the presence of tiny pores observed on the particles of the $BaZr_xTi_{(1-x)}O_3$ has been established to be advantageous for the piezoelectric response of piezoelectric materials.[58] The morphologies of the piezoelectric materials were further probed by HRTEM (Fig. 1g–i). The irregular shapes observed for $BaTiO_3$ was clearly validated by Fig. 1g. Moreover, Fig. 1h and i reveal the gradual transformation of $BaZr_{(x)}Ti_{(1-x)}O_3$ particles from the irregular $BaTiO_3$ shape to a more consistent globular structure as the composition of Zr increases in the crystal structure of the $BaZr_{(x)}Ti_{(1-x)}O_3$.

3.2 Electrochemical characterization of the fabricated piezoelectric electrode

Cyclic voltammetry of the electrodes was performed in a solution of 5 mM $[Fe(CN)_6]^{3-/4-}$ redox probe containing 0.1 M KCl (Fig. 2a). The effect of the addition of Zr is noticed by the increase in the anodic and cathodic peak current of the redox probe. The highest anodic peak current value of 1.03×10^{-3} A was obtained upon using FTO/$BaZr_{(0.1)}Ti_{(0.9)}O_3$ electrode, while lower peak current values of 9.52×10^{-4} A and 7.94×10^{-4} A, were obtained for FTO/$BaZr_{(0.05)}Ti_{(0.95)}O_3$ and FTO/$BaTiO_3$ electrodes, respectively. This implies that the electroactive performance in the redox species and the oxidative ability of the piezoelectric materials increased as the composition of Zr in $BaZr_{(x)}Ti_{(1-x)}O_3$ increased, which facilitated a better facile electron transfer in the redox probe. Hence, FTO/$BaZr_{(0.1)}Ti_{(0.9)}O_3$ electrode is expected to be more efficient towards electrochemical and SEC oxidation of the pollutant.

Electrochemical impedance spectroscopy was also carried out to further establish the electroactive behaviour of the electrodes. This was conducted in a 5 mM $[Fe(CN)_6]^{3-/4-}$ solution

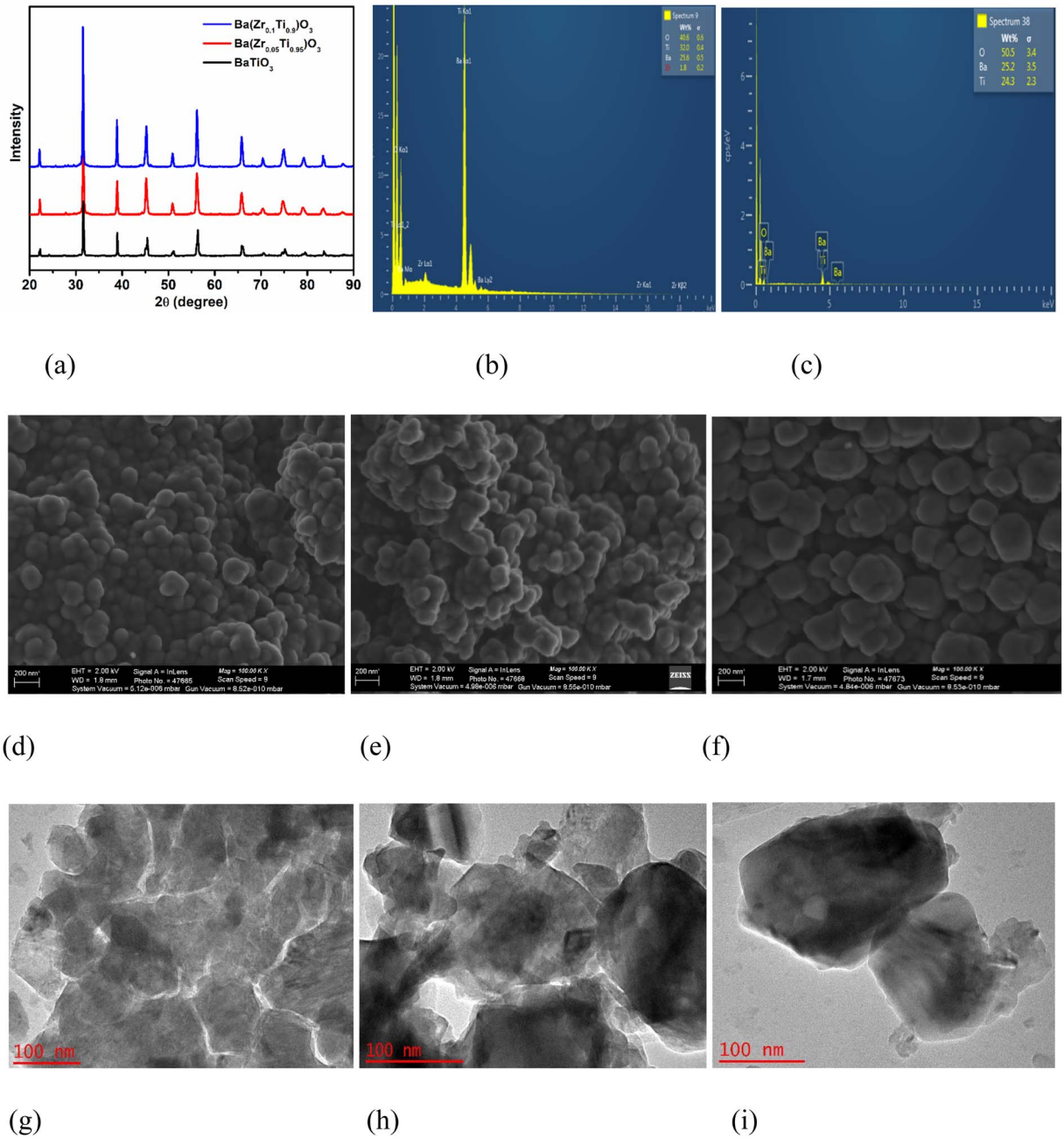

Fig. 1 (a) X-ray diffractogram of the piezoelectric materials, (b) EDS spectrum of $BaZr_{(0.1)}Ti_{(0.9)}O_3$, FESEM images of (c) $BaTiO_3$ (d) $BaZr_{(0.05)}$-$Ti_{(0.95)}O_3$, (e) $BaZr_{(0.1)}Ti_{(0.9)}O_3$, HRTEM images of (f) $BaTiO_3$, (g) $BaZr_{(0.05)}Ti_{(0.95)}O_3$, (h) $BaZr_{(0.1)}Ti_{(0.9)}O_3$, (i) $BaZr_{(x)}Ti_{(1-x)}O_3$.

containing 0.1 M KCl within a frequency range of 10^5 to 10^{-2} Hz. From the Nyquist plot obtained (Fig. 2b), charge transfer resistance (R_{ct}) of 57 Ω, 103 Ω and 151 Ω were obtained for FTO/$BaZr_{(0.1)}Ti_{(0.9)}O_3$, FTO/$BaZr_{(0.05)}Ti_{(0.95)}O_3$ and FTO/$BaTiO_3$, respectively. Since the occurrence of a small arc radius indicates a lessened resistance or difficulty to the transport of charged particles across the electrode and analyte solution interface, increased mass transport of charged particles across the bulk solution is expected on FTO/$BaZr_{(0.1)}Ti_{(0.9)}O_3$ electrode. This further translates to an improved interaction between the generated reactive species at the electrode surface and the analyte in the bulk solution when FTO/$BaZr_{(0.1)}Ti_{(0.9)}O_3$ is applied for SEC oxidation of the analyte.

The transient sonoelectrochemical current density of the electrodes obtained in the presence of 40 W ultrasound power and 2.0 V bias potential, while keeping the electrode at 15 mm distance from the probe, is presented in Fig. 2c. The highest sonocurrent density (j) value of 2.33 mA cm^{-2} was obtained for the FTO/$BaZr_{(0.1)}Ti_{(0.9)}O_3$ electrode. This indicates that the piezoelectric effect increases upon incorporating Zr into the $BaTiO_3$ structure. The increase in the sonocurrent response observed for FTO/$BaZr_{(0.1)}Ti_{(0.9)}O_3$ further suggests an

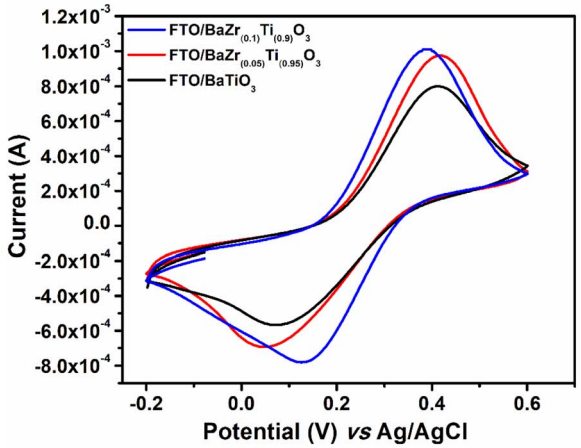

(a)

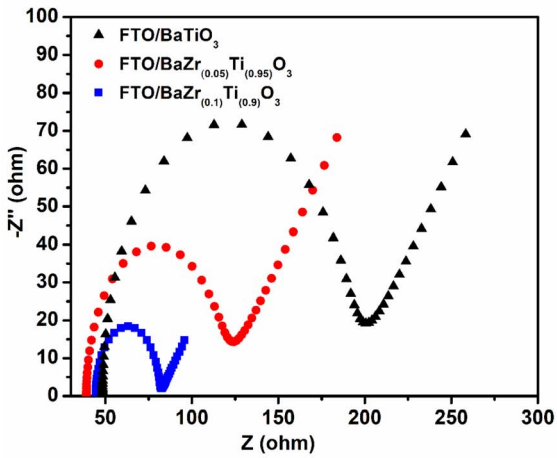

(b)

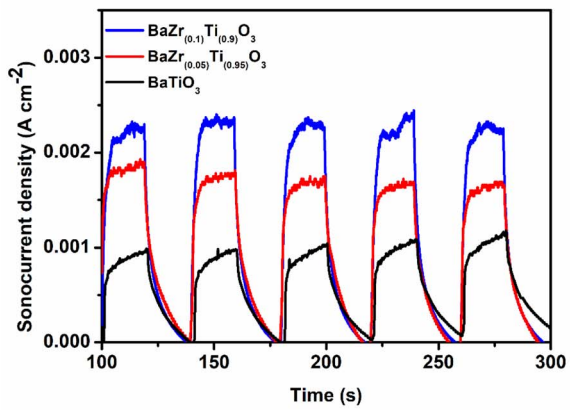

(c)

Fig. 2 (a) Cyclic voltammogram at scan rate of 100 mV s^{-1}, (b) Nyquist plot at 10^5 Hz to 10^{-2} Hz and bias potential of 0.21 V for all the prepared electrodes, (c) transient sonoelectrochemical current density response at 2.0 V bias potential.

enhancement in the generation and migration of the piezo polarized charges to the surface of the material as a result of the incorporation of Zr into the $BaTiO_3$ crystal structure.[57] Furthermore, the notable current output observed for the electrode was influenced by acoustic streaming effect, which promoted mass transfer in the medium through the presence of ultrasound waves. Acoustic cavitation effect induced by the presence of ultrasound also impacted the current output through the formation of microjet and shockwave which helps to prevent the passivation at the electrode surface.[59] Moreover, improvement in the piezo polarized effect and charges at the surface of the material will translate to an improved generation of reactive species in the SEC system and ultimately improve the rate of decomposition of SMX.

3.3 Sonocatalysis and electrochemical oxidation of SMX

The trend of degradation of SMX in the synthetic wastewater is presented in Fig. 3. Sonocatalysis of SMX performed in the presence of each electrode (Fig. 3a) shows that sonocatalysis in the presence of FTO/$BaZr_{(0.1)}Ti_{(0.9)}O_3$ has the best performance with a degradation efficiency of 46.62%. Moreover, the degradation efficiency of 39.59% (FTO/$BaZr_{(0.05)}Ti_{(0.95)}O_3$) and 30.40% (FTO/$BaTiO_3$) were also obtained during this process. This trend suggests an improvement in the activation of piezo-polarized charges within the $BaZr_{(x)}Ti_{(1-x)}O_3$ particle with increasing composition of Zr.[48] Improvement in the formation of piezo-polarized charges will favour easy and quick formation of reactive species responsible for the decomposition of SMX. Moreover, the acoustic streaming and cavitation effect played a significant role in the degradation of SMX by enhancing mass transfer and maintaining the continuous activity of the electrode through continuous cleaning of the electrode surface.

Similar trend was obtained for the electrochemical oxidation of SMX in simulated wastewater on the electrodes (Fig. 3b). Herein, the lowest concentration degradation efficiency of 13.39% was obtained for FTO/$BaTiO_3$. This is typical of ceramic materials possessing high dielectric constant and high tendency of oxide layer formation during electrochemical reactions like $BaTiO_3$.[54,60,61] However, upon the incorporation of Zr, the degradation efficiency increased to 20.36% (FTO/$BaZr_{(0.05)}Ti_{(0.95)}O_3$) and 24.85% (FTO/$BaZr_{(0.1)}Ti_{(0.9)}O_3$), which indicates an improvement in the direct oxidation of SMX as earlier observed in the CV of the electrodes. However, the low degradation efficiency obtained during electrochemical oxidation suggests that the decomposition of SMX occurred predominantly through indirect oxidation route.

3.4 Sonoelectrochemical oxidation of SMX

SEC oxidation technique, which employs the synergistic effect of combining sonocatalysis and electrochemical oxidation for the decomposition of SMX in simulated wastewater, was also carried out and presented in Fig. 3c. Degradation efficiencies of 86.16%, 76.08% and 61.57% were obtained from FTO/$BaZr_{(0.1)}Ti_{(0.9)}O_3$, FTO/$BaZr_{(0.05)}Ti_{(0.95)}O_3$ and FTO/$BaTiO_3$ electrodes, respectively. Firstly, this shows that combining sonocatalysis and electrochemical oxidation was favourable for the

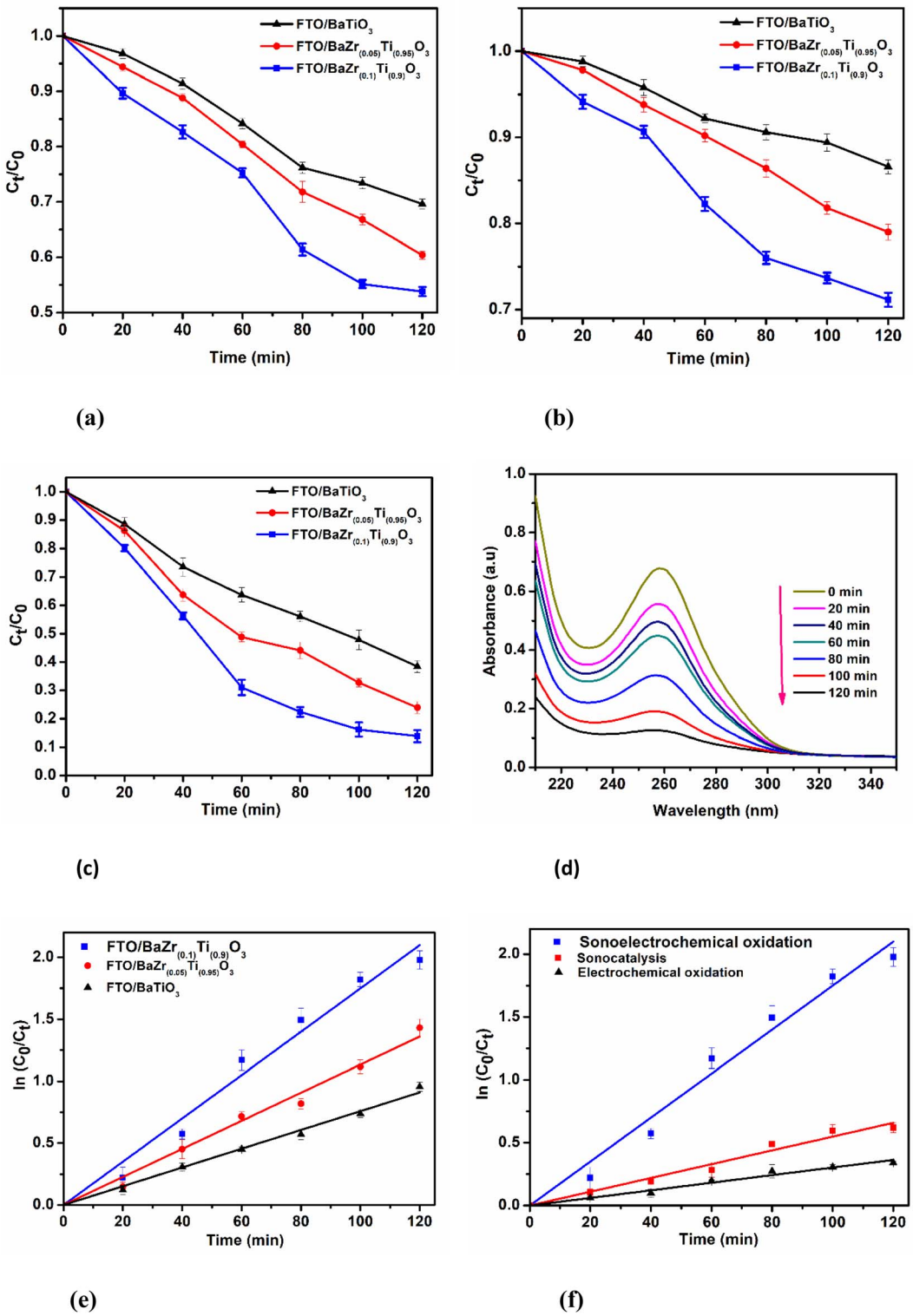

Fig. 3 Degradation efficiency plots for (a) sonocatalysis of SMX at 40 W ultrasound power and 15 mm electrode-probe distance, (b) electrochemical oxidation of SMX at 2 V bias potential, (c) SEC oxidation of SMX in 0.1 M Na_2SO_4 electrolyte solution, (d) absorption spectra of SMX obtained at a successive time interval during SEC oxidation on FTO/$BaZr_{(0.1)}Ti_{(0.9)}O_3$ electrode, (e) reaction kinetics plots comparing SEC oxidation of SMX on the electrodes, (f) reaction kinetics plot comparing each technique on FTO/$BaZr_{(0.1)}Ti_{(0.9)}O_3$ electrode in simulated wastewater.

decomposition of organic pollutants in wastewater.[52,62] This advantage can be attributed to processes such as acoustic cavitation and acoustic streaming effects,[63] which governs physical effect involving the nucleation and collapse of microbubble, shockwave and microjet formation, mass transport characteristics of particle in an aqueous medium.[64,65] These

effects are largely responsible for the perpetual cleaning of the electrode surface and thinning of the electrode analyte solution-electrode boundary, thereby improving the migration of charged particles and the pollutant across the electrode solution interface in the bulk solution.[66,67] Secondly, it is again apparent that the incorporation of Zr into the $BaTiO_3$ improved the SEC response of the barium titanate with the higher Zr mole ratio performing better. Thus, the improvement in the generation of piezo-polarized charge in the $BaZr_{(0.1)}Ti_{(0.9)}O_3$ aided the production of more reactive species responsible for the non-selective decomposition of SMX in the system. The absorption spectra showing the trend degradation during SEC oxidation of SMX in simulated wastewater, obtained at successive time intervals is presented in Fig. 3d.

To further verify the piezo-polarized effect on the overall efficiency of SMX, TiO_2 (with non-piezo-polarizable domain)[68] was also immobilized of FTO and applied for sonocatalysis, electrochemical oxidation and SEC oxidation of SMX in simulated wastewater. These results were compared with the performance of FTO/$BaZr_{(0.1)}Ti_{(0.9)}O_3$ electrode and presented in Fig. S1.† A marginal increase to 19.83% degradation efficiency was observed for sonocatalytic degradation of SMX on FTO/TiO_2 electrode from 15.17% obtained for sonolysis of SMX (without electrode). These minimal degradation efficiencies can be attributed to the collapse of microbubbles formed in the bulk solution, resulting in the pyrolytic breakage of water molecule and the formation of hydroxyl radical[24] as the only notable reaction responsible for these performances, even in the presence of FTO/TiO_2 electrode. Moreover, the wide difference in the degradation efficiency of SMX using FTO/TiO_2 electrode (39.40%) and FTO/$BaZr_{(0.1)}Ti_{(0.9)}O_3$ electrode (86.16%) during SEC oxidation as well as FTO/TiO_2 electrode (19.83%) and FTO/$BaZr_{(0.1)}Ti_{(0.9)}O_3$ electrode (46.69%) obtained during sonocatalytic oxidation processes further validate the imposing impact of the piezo-potential effect of FTO/$BaZr_{(0.1)}Ti_{(0.9)}O_3$ electrode on the overall removal of SMX.

3.5 Kinetics and synergistic studies

The reaction kinetics for SEC oxidation, sonocatalysis and electrochemical oxidation techniques, calculated from Fig. 3e, f and S2,† all conform to a pseudo first-order reaction as the kinetic plots fitted into the formula $k_t = \ln(C_0/C_t)$.[52] Where k, t, C_0 and C_t represent the rate constant (min^{-1}), time (min), initial concentration (mg L^{-1}) and concentration at a given time (mg L^{-1}), respectively. From the kinetic plot obtained for the SEC oxidation of SMX on each electrode (Fig. 3e), the highest rate constant value of 1.75×10^{-2} min^{-1} ($R^2 = 0.9763$) was obtained for FTO/$BaZr_{(0.1)}Ti_{(0.9)}O_3$ electrode. However, 1.13×10^{-2} min^{-1} ($R^2 = 0.9949$) and 7.58×10^{-3} min^{-1} ($R^2 = 0.9973$) were the rate constant values obtained for FTO/$BaZr_{(0.05)}Ti_{(0.95)}O_3$ FTO/$BaTiO_3$ electrodes, respectively. This trend represents a 2.3 fold (FTO/$BaZr_{(0.1)}Ti_{(0.9)}O_3$) and 1.5 fold (FTO/$BaZr_{(0.05)}Ti_{(0.95)}O_3$) increment from the degradation rate obtained for FTO/$BaTiO_3$ electrode, which further reinforces an improvement in the piezo-polarized activity of FTO/$BaZr_{(0.1)}Ti_{(0.9)}O_3$ electrode towards the generation of reactive species responsible for the decomposition of SMX in the system.

As expected, apparent rate constants for SMX degradation were lower for sonocatalysis [5.49×10^{-3} min^{-1} ($R^2 = 0.9901$)] and electrochemical oxidation [3.03×10^{-3} min^{-1} ($R^2 = 0.9922$)] than that of SEC [1.75×10^{-2} min^{-1} ($R^2 = 0.9921$)] on FTO/$BaZr_{(0.1)}Ti_{(0.9)}O_3$ electrode (Fig. 3f).

The synergistic index of combining sonocatalysis with electrochemical oxidation during SEC oxidation was estimated with eqn (3).[69]

$$S = \frac{k_{SEC}}{k_s + k_{EC}} \quad (3)$$

where k_{SEC}, k_s and k_{EC} represents rate constants for SEC oxidation, sonocatalysis and electrochemical oxidation, respectively.[70] A positive synergistic index of 2.053, obtained for SEC oxidation of SMX on FTO/$BaZr_{(0.1)}Ti_{(0.9)}O_3$ electrode, shows that the combination of sonocatalysis and electrochemical oxidation produced far reaching effects than the individual methods.[52] Estimated rate constant for other electrodes followed similar trend as FTO/$BaZr_{(0.1)}Ti_{(0.9)}O_3$ electrode for all the processes as presented in Fig. S2.† Moreover, the action of acoustic cavitation and acoustic streaming improved the reaction kinetics of SEC oxidation process through continuous cleaning of the electrode surface and improved mass transfer, respectively occasioned by the presence of ultrasound waves in the system. The comparative study of the degradation efficiencies of SMX on each electrode and their estimated rate constant obtained for each degradation technique presented in Table 1, further reveals the increasing impact of the piezo-polarization effect on the overall performance of SEC oxidation process with increasing amount of Zr ion in $BaZr_xTi_{(1-x)}O_3$ materials.

3.6 Total organic carbon analysis

Analysis to further investigate the extent of decomposition of SMX in simulated wastewater and actual effluent (obtained from Daspoort WWTP, Pretoria) spiked with 5 mg L^{-1} of SMX

Table 1 Comparative study of each technique showing the degradation efficiencies and rate constant of the electrodes

	Technique/degradation efficiency (%)			Rate constant (min^{-1})		
Electrode	SEC oxidation	Sonocatalysis	Electrochemical oxidation	SEC oxidation	Sonocatalysis	Electrochemical oxidation
$BaZr_{(0.1)}Ti_{(0.9)}O_3$	88.16	46.62	24.85	1.75×10^{-2}	5.49×10^{-3}	3.03×10^{-3}
$BaZr_{(0.05)}Ti_{(0.95)}O_3$	76.08	39.59	20.36	1.13×10^{-2}	4.32×10^{-3}	2.05×10^{-3}
$BaTiO_3$	61.57	30.40	13.39	7.58×10^{-3}	3.25×10^{-3}	1.23×10^{-3}

are reported in Fig. 4. TOC removal efficiency obtained in both simulated and actual wastewater spiked with SMX maintained trends similar to the degradation efficiency for all the electrodes. The degradation trend obtained for the TOC removal is also similar to those obtained for the concentration decay of SMX using UV/vis spectrophotometer. In Fig. 4a, 63.61% TOC removal efficiency was obtained as the best TOC removal efficiency for FTO/$BaZr_{(0.1)}Ti_{(0.9)}O_3$ electrode during SEC oxidation of SMX in simulated wastewater. However, the TOC removal efficiency gradually decreased from 58.18% to 32.86% upon applying FTO/$BaZr_{(0.05)}Ti_{(0.95)}O_3$ and FTO/$BaTiO_3$ electrodes, respectively. This further confirms the occurrence of improved piezo-polarized effect in the system on FTO/$BaZr_{(0.1)}Ti_{(0.9)}O_3$ electrode as the composition of Zr in BZT increases. The synergy of combining both sonocatalysis and electrochemical oxidation during SEC oxidation was further confirmed in Fig. 4b. Here, TOC removal efficiencies of 24.31% obtained during sonocatalysis and 11.93% during electrochemical oxidation on FTO/$BaZr_{(0.1)}Ti_{(0.9)}O_3$ electrode were less impressive compared to 63.61% obtained during SEC oxidation of SMX from simulated wastewater. Mass transfer and continuous activation of the electrode surface occasioned by respective effects of acoustic streaming and acoustic cavitation also contributed to the overall performance of the SEC process. A similar performance was observed with the degradation of SMX spiked actual wastewater for SEC oxidation as follows: FTO/$BaZr_{(0.1)}Ti_{(0.9)}O_3$ (41.47%), FTO/$BaZr_{(0.05)}Ti_{(0.95)}O_3$ (33.83%) and FTO/$BaTiO_3$ (27.80%) as presented in Fig. 4c. The results in both simulated and actual wastewater further confirm SEC oxidation, a synergy of sonocatalysis and electrochemical oxidation, can be an effective technique for the treatment of recalcitrant organics in water. Moreover, TOC removal efficiency of 18.11% (sonocatalysis) and 4.51% (electrochemical oxidation) in Fig. 4d were obtained for the SMX spiked actual effluent. The reduction in the TOC removal from the spiked actual wastewater in

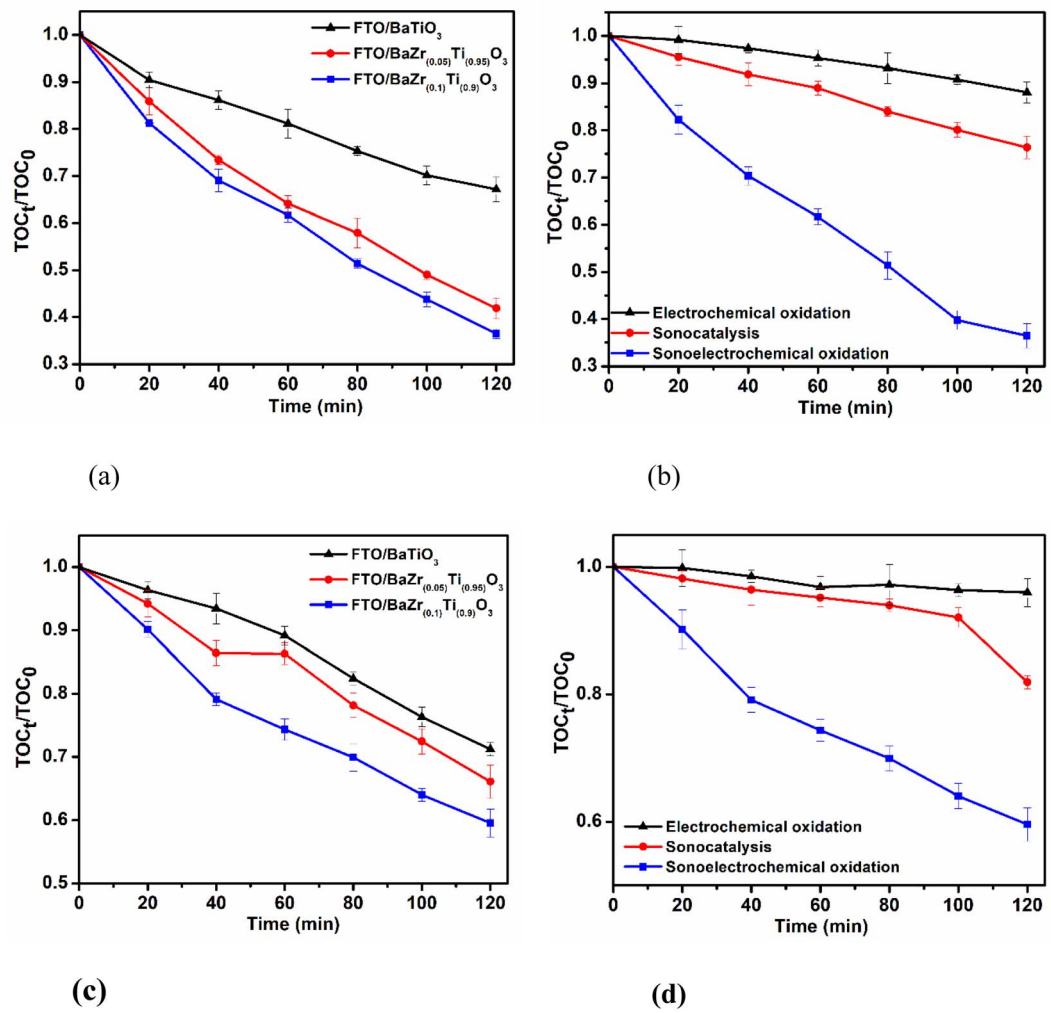

Fig. 4 TOC removal efficiency plot for (a) SEC oxidation on FTO/$BaZr_{(0.1)}Ti_{(0.9)}O_3$ FTO/$BaZr_{(0.05)}Ti_{(0.95)}O_3$ FTO/$BaTiO_3$ electrodes, (b) sonocatalysis, electrochemical oxidation and SEC oxidation of SMX on FTO/$BaZr_{(0.1)}Ti_{(0.9)}O_3$ in simulated wastewater, containing 0.1 M Na_2SO_4, (c) SEC oxidation on FTO/$BaZr_{(0.1)}Ti_{(0.9)}O_3$, FTO/$BaZr_{(0.05)}Ti_{(0.95)}O_3$, FTO/$BaTiO_3$ electrodes, (d) sonocatalysis, electrochemical oxidation and SEC oxidation on FTO/$BaZr_{(0.1)}Ti_{(0.9)}O_3$ electrode of SMX spiked actual wastewater containing 0.1 M Na_2SO_4.

comparison to the simulated wastewater may be attributed to the presence of other recalcitrant organic matter in the former.

3.7 Scavenger, reusability and proposed mechanism of the SEC oxidation process

Scavenger study is aimed at investigating the dominant reactive species accountable for the non-selective degradation of SMX during the SEC oxidation process on the FTO/$BaZr_{(0.1)}Ti_{(0.9)}O_3$ electrode. Terephthalic acid (TA) and tertiary butanol (*t*-BuOH) were chosen as scavengers to trap hydroxyl radical ($^{\bullet}OH$)[34,71] while *p*-benzoquinone (*p*-BQ)[46,72] and sodium azide (NaN_3)[73,74] were used as scavengers for superoxide radical ($O_2^{\bullet-}$) radical and singlet oxygen ($^1O_2$) respectively (Fig. 5a). Notable reduction in the percentage degradation from 86.16% to 27.31% in the presence of TA and 47.63% in the presence of *t*-BuOH show that $^{\bullet}OH$ played a predominant role in the degradation of SMX in the SEC system. This is expected as $^{\bullet}OH$ radical has been proven to be the most dominant reactive specie in every sonochemical reaction.[75] $O_2^{\bullet-}$ and $^1O_2$ also contributed to the overall degradation process during SEC oxidation as indicated by a decrease in the degradation efficiency to 52.38% and 77.47% of the SEC process in the presence of *p*-BQ and NaN_3 respectively. However, the short life span of $^1O_2$ has been suggested as the factor limiting its degradation activity.[76] In addition, the estimated reaction rate of the SEC oxidation process in the presence of each oxidant's trapping agent all conforms to a pseudo first order kinetics and are presented in Fig. 5b. A significant reduction in the rate constants of SEC process in the presence of TA [4.79×10^{-3} min^{-1} ($R^2 = 0.9553$)] and *t*-BuOH [9.05×10^{-3} min^{-1} ($R^2 = 0.9885$)] from rate constant in the absence of scavengers [1.75×10^{-2} min^{-1} (0.9723)] further confirms the predominance of $^{\bullet}OH$ in breaking down of SMX in the system. Compared with inhibitory activity of TA, *t*-BuOH has a weaker inhibitory activity[34] as indicated by the outstanding 3.5-fold decrease in the rate constant with TA as against a 2-fold decrease observed with *t*-BuOH as scavenger. Moreover, a 1.6

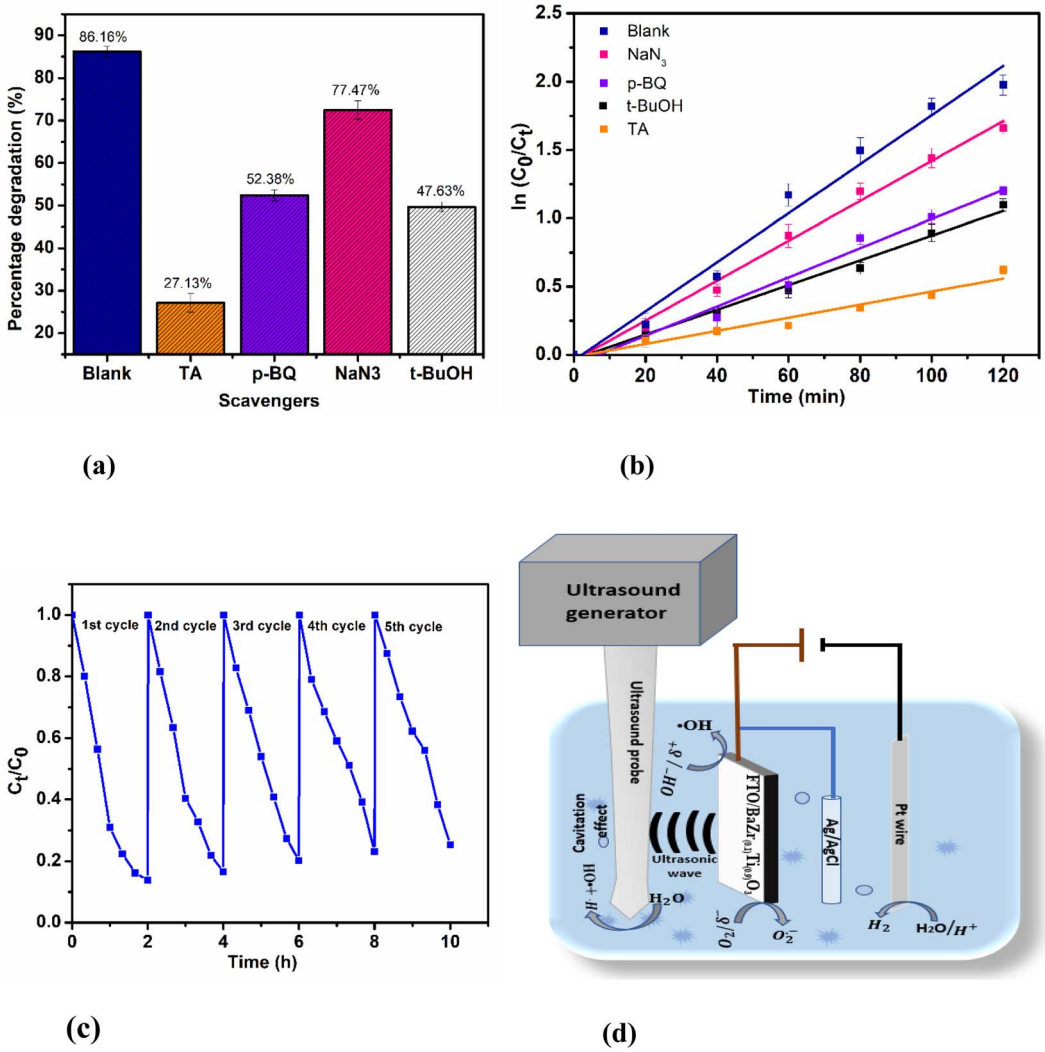

Fig. 5 (a) Scavenger study plot for the SEC oxidation of SMX on FTO/$BaZr_{(0.1)}Ti_{(0.9)}O_3$ electrode in the presence and absence of trapping agents, (b) reusability plot for the SEC oxidation of SMX on FTO/$BaZr_{(0.1)}Ti_{(0.9)}O_3$ electrode, (c) diagrammatic representation of the SEC oxidation system (d) proposed reaction scheme using FTO/$BaZr_{(0.1)}Ti_{(0.9)}O_3$ electrode.

fold decrease in the rate constant obtained in the presence of *p*-BQ [1.07×10^{-2} min^{-1} (0.9808)] and 1.1 fold with NaN_3 [1.56×10^{-2} min^{-1} (0.9908)] also confirms the importance of $O_2^{\cdot-}$ and $^1O_2$ in the degradation process. Other than the piezo-generation route for the production of $^{\cdot}OH$ radical in the SEC system, chemical effect of ultrasound that results in the pyrolytic cleavage of water molecules during the implosion of micro-bubble also contributed to the impact of $^{\cdot}OH$ radical during the SEC process.

The reusability plot presented in Fig. 5c, shows that FTO/$BaZr_{(0.1)}Ti_{(0.9)}O_3$ electrode displayed moderate stability towards the SEC degradation of SMX in synthetic wastewater after five cycles, as 74.44% degradation efficiency was obtained after the fifth cycle. The downward trend in the efficiency of the electrode obtained after each cycle may be attributed to the negligible wearing off of the material, arising from the prolonged exposure of ultrasound to the electrode surface. The possible impact of leaching of the material into the solution after the SEC process was performed using inductively coupled plasma optical emission spectrometer (ICP-OES). Trace concentrations of barium and titanium detected by ICPOES were below the detection limit (1 mg L^{-1}) set by the European union[77] after the SEC process (Fig. S3†), thereby preventing further environmental pollution. However, the electrode showed impressive stability towards the ultrasound exposed to it during the SEC process.

The proposed reaction scheme of the SEC oxidation on the FTO/$BaZr_{(0.1)}Ti_{(0.9)}O_3$ electrode is represented in Fig. 5d. The reaction mechanism applies to all electrodes used for this work since they all possess piezoelectric properties. As earlier discussed, the piezoelectric properties of the materials applied as electrodes are often activated by a mechanical agitation effect. Ultrasound waves from the probe irradiated into the SEC system played this important role. Since the electrode was positioned parallel (at 15 mm distance) to the ultrasound probe (operating at 40 W ultrasound power), the ultrasonic wave reaching the electrode surface aids the activation of band bending within the crystal structure of the material. This band bending causes the displacement of stable dipoles and the generation of opposite polarized charges within the material.[36,38,49,78] These polarized charges migrate in opposite directions to the surface of the piezoelectric material in a process referred to as internal polarization.[45,47,49] Subsequently, these dipole charges interact with hydroxyl ion as well as dissolved oxygen to generate hydroxyl radical ($^{\cdot}OH$) and superoxide radical ($O_2^{\cdot-}$).[39,43,47] Eqn (4)–(6) support the formation of highly reactive oxidants in the system by the electrodes.[39,43,45]

$$BaZr_{(0.1)}Ti_{(0.9)}O_3 + \text{ultrasound} \rightarrow BaZr_{(0.1)}Ti_{(0.9)}O_3\ (\delta^+, \delta^-) \quad (4)$$

$$BaZr_{(0.1)}Ti_{(0.9)}O_3\ (\delta^+) + OH^- \rightarrow {}^{\cdot}OH \quad (5)$$

$$BaZr_{(0.1)}Ti_{(0.9)}O_3\ (\delta^-) + O_2 \rightarrow O_2^{\cdot-} \quad (6)$$

where δ^+ and δ^- are the generated piezo-polarized charges.

In addition, the ultrasound wave helps to prevent the passivation of the electrode surface through a phenomenon known as acoustic cavitation.[63] Ultrasound effect in the system also causes thinning of the electrode-analyte solution boundary, thereby enhancing easy migration of both analyte and charged particles to the electrode surface and across the bulk solution referred to as acoustic streaming. Furthermore, acoustic cavitation induced by ultrasound effect causes water molecules to split homolytically, thereby resulting in the generation of $^{\cdot}OH$ and $H^{\cdot}$ in the process.[26,29] The continuous mixing effect also influenced by the presence of ultrasound in the system enhances unrelentless collision of the generated reactive oxidants in the SEC system with the target pollutant. Though the oxidation of the pollutant was considered to predominantly occur through the indirect route, the low degradation efficiency obtained during electrochemical oxidation method predicts the occurrence of minimal direct oxidation on the electrode, which occurred through the application of bias potential. Eqn (7)–(13) represent other reactions taking place in the SEC system.[23,79]

$$H_2O \rightarrow {}^{\cdot}OH + H^+ + e^- \quad (7)$$

$$O_2 + e^- \rightarrow O_2^{\cdot-} \quad (8)$$

$$O_2 + H^{\cdot} \rightarrow HO_2^{\cdot} \quad (9)$$

$$H^{\cdot} + HO_2^{\cdot} \rightarrow H_2 + {}^1O_2 \quad (10)$$

$$2HO_2^{\cdot} \rightarrow H_2O_2 + O_2 \quad (11)$$

$$H_2O +))))\ (\text{ultrasound}) \rightarrow {}^{\cdot}OH + H^{\cdot} \quad (12)$$

$$SMX + \left({}^{\cdot}OH,\ O_2^{\cdot-}\right) \rightarrow \text{byproducts} + CO_2 + H_2O \quad (13)$$

3.8 Proposed reaction pathway for the decomposition of SMX on FTO/$BaZr_{(0.1)}Ti_{(0.9)}O_3$ electrode

Proposed reaction pathway for the degradation of SMX on FTO/$BaZr_{(0.1)}Ti_{(0.9)}O_3$ electrode in the SEC oxidation system was investigated. The byproducts from the decomposition of SMX were obtained from the chromatograms of UPLC-MS analysis of the SMX standard solution, SMX spiked effluent and aliquots were withdrawn from the SEC system during the degradation at different times are also presented in Fig. S4.† The standard solution of SMX clearly displayed a distinct peak at 4.95 min ($m/z = 254$). In addition, resulting byproducts formed during the decomposition of SMX for 120 min were identified using the various ion peaks indicated on the chromatograms are presented in Fig. 6. Paramount byproducts identified from the mass spectra obtained for SMX decomposition include $m/z = 290$, $m/z = 283$, $m/z = 276$, $m/z = 247$ and $m/z = 239$, $m/z = 226$, $m/z = 164$, $m/z = 116$. Three possible decomposition pathways are proposed from these intermediates identified on the spectra obtained for both synthetic and effluent wastewater containing the target pollutant. Pathway 1 (ABCDE) involves the hydroxylation and acetylation (reaction of hydroxyl and alkyl radicals with SMX) of the compound. This was followed by the opening of the isoxazole ring and demethylation reaction as observed in C. Furthermore, the opened isoxazole ring experienced dehydroxylation and cleavage of the amino group attached to the

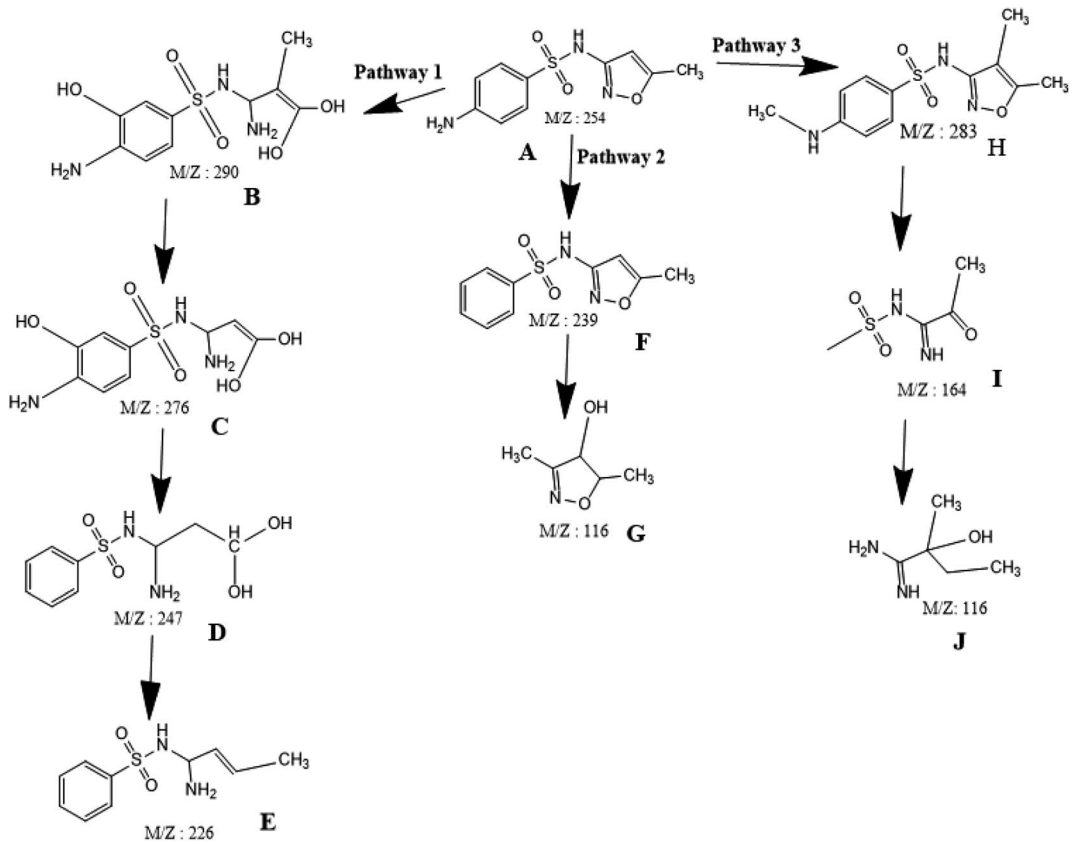

Fig. 6 Proposed decomposition pathway and intermediates formed during the SEC oxidation of SMX on FTO/$BaZr_{(0.1)}Ti_{(0.9)}O_3$ electrode.

benzene ring as earlier reported.[80,81] Pathway 2 (AFG) possibly occurred through the cleavage of the methyl group attached to the benzene ring as observed in F. This was followed by the cleavage of the benzene sulfonamide and the amino groups, leaving the isoxazole group to further undergo hydroxylation and methylation reactions[80,82] as noticed in G. Also, pathway 3 (AHIJ) involves the acetylation of the amino group attached to the benzene ring as well as the isoxazole group. The methylated secondary amine attached to the sulfonamide on the isoxazole group was further replaced with a single methyl group as observed in I. Additionally, the isoxazole ring experienced oxidation in the same step, causing the opening of the ring and the formation of a ketone group attached to the sulfonamide in I. Moreover, the ketone group and the amine moiety experienced further oxidation, resulting in the cleavage of the sulfonyl group[80,82,83] and the formation of an alcohol entity. Notably, the possible reaction pathways stated above were influenced by the presence of the highly unstable reactive species generated in the SEC system, which can further influence the decomposition of the intermediate products to byproducts such as H_2O, SO_4^{2-}, CO_2, NH_4^+.

4 Conclusion

The piezoelectric materials were successfully synthesized and immobilized on the substrate (FTO glass). The electrodes showed varying piezoelectric responses to ultrasound effect in the SEC system with FTO/$BaZr_{(0.1)}Ti_{(0.9)}O_3$ electrode displaying the highest current output and lowest charge transfer resistance as observed in the sonocurrent response and the Nyquist plots of the electrodes. With operating conditions of 40 W ultrasound power, 2 V bias potential and 15 mm electrode probe distance, FTO/$BaZr_{(0.1)}Ti_{(0.9)}O_3$ electrode displayed the best efficiency toward the SEC oxidation of SMX both in simulated wastewater and actual wastewater spiked with SMX. Furthermore, $^{\bullet}OH$ was determined to be the most predominant reactive specie carrying out the decomposition of SMX in the SEC system non-selectively. This was substantiated by a sharp reduction in the degradation efficiency of FTO/$BaZr_{(0.1)}Ti_{(0.9)}O_3$ electrode upon the introduction of terephthalic acid as $OH^{\bullet}$ inhibiting agent from 86.16% (without inhibitor) to 27.31% (with inhibitor). Furthermore, byproducts obtained after the decomposition of SMX revealed that the FTO/$BaZr_{(0.1)}Ti_{(0.9)}O_3$ electrode was effective towards the decomposition of SMX in the bulk solution. The findings from the work, therefore present sonoelectrochemical oxidation as a reliable AOP alternative for the treatment of various organic polluted wastewater.

Conflicts of interest

The authors declare that they have no known competing financial interests or personal relationships that could have appeared to influence the work reported in this paper.

Acknowledgements

We immensely appreciate the financial support received towards this research from the following South African organizations: National Research Foundation (NRF CSUR grant number SRUG200326510622), Faculty of Science, University of Johannesburg; Centre for Nanomaterials Science Research (CNSR), University of Johannesburg; and Water Research Commission (WRC).

References

1 M. Mezzelani, S. Gorbi and F. Regoli, *Mar. Environ. Res.*, 2018, **140**, 41–60.
2 L. M. Madikizela, N. T. Tavengwa and L. Chimuka, *J. Environ. Manage.*, 2017, **193**, 211–220.
3 M. Xu, H. Huang, N. Li, F. Li, D. Wang and Q. Luo, *Ecotoxicol. Environ. Saf.*, 2019, **175**, 289–298.
4 M. Patel, R. Kumar, K. Kishor, T. Mlsna, C. U. Pittman and D. Mohan, *Chem. Rev.*, 2019, **119**, 3510–3673.
5 M. Liu, H. Yin and Q. Wu, *Ecotoxicol. Environ. Saf.*, 2019, **183**, 109497.
6 D. Xu, Y. Xie and J. Li, *Ecotoxicol. Environ. Saf.*, 2022, **232**, 113258.
7 L. M. Madikizela, S. Ncube and L. Chimuka, *J. Environ. Manage.*, 2020, **253**, 109741.
8 R. A. Mole and B. W. Brooks, *Environ. Pollut.*, 2019, **250**, 1019–1031.
9 S. Fekadu, E. Alemayehu, R. Dewil and B. Van der Bruggen, *Sci. Total Environ.*, 2019, **654**, 324–337.
10 O. F. S. Khasawneh and P. Palaniandy, *Process Saf. Environ. Prot.*, 2021, **150**, 532–556.
11 C. F. Couto, L. C. Lange and M. C. S. Amaral, *J. Water Process. Eng. J*, 2019, **32**, 100927.
12 P. Chaturvedi, P. Shukla, B. S. Giri, P. Chowdhary, R. Chandra, P. Gupta and A. Pandey, *Environ. Res.*, 2021, **194**, 110664.
13 Y. Yang, Y. S. Ok, K. H. Kim, E. E. Kwon and Y. F. Tsang, *Sci. Total Environ.*, 2017, **596–597**, 303–320.
14 D. Kanakaraju, B. D. Glass and M. Oelgemöller, *J. Environ. Manage.*, 2018, **219**, 189–207.
15 S. J. Mazivila, I. A. Ricardo, J. M. M. Leitão and J. C. G. Esteves da Silva, *Trends Environ. Anal. Chem.*, 2019, **24**, 1–10.
16 A. Giwa, A. Yusuf, H. A. Balogun, N. S. Sambudi, M. R. Bilad, I. Adeyemi, S. Chakraborty and S. Curcio, *Process Saf. Environ. Prot.*, 2021, **146**, 220–256.
17 O. A. Arotiba, B. O. Orimolade and B. A. Koiki, *Curr. Opin. Electrochem.*, 2020, **22**, 25–34.
18 B. N. Zwane, B. O. Orimolade, B. A. Koiki, N. Mabuba, C. Gomri, E. Petit, V. Bonniol, G. Lesage, M. Rivallin, M. Cretin and O. A. Arotiba, *Water*, 2021, **13**, 2772.
19 B. Huang, Z. Wu, H. Zhou, J. Li, C. Zhou, Z. Xiong, Z. Pan, G. Yao and B. Lai, *J. Hazard. Mater.*, 2021, **412**, 125253.
20 G. Başaran Dindaş, Y. Çalişkan, E. E. Çelebi, M. Tekbaş, N. Bektaş and H. C. Yatmaz, *J. Environ. Chem. Eng.*, 2020, **8**, 103777.
21 J. Wang and S. Wang, *Chem. Eng. J.*, 2020, **401**, 126158.
22 B. Thokchom, A. B. Pandit, P. Qiu, B. Park, J. Choi and J. Khim, *Ultrason. Sonochem.*, 2015, **27**, 210–234.
23 A. Hassani, M. Malhotra, A. V. Karim, S. Krishnan and P. V. Nidheesh, *Environ. Res.*, 2022, **205**, 112463.
24 J. Theerthagiri, J. Madhavan, S. J. Lee, M. Y. Choi, M. Ashokkumar and B. G. Pollet, *Ultrason. Sonochem.*, 2020, **63**, 104960.
25 W. R. P. Barros, J. R. Steter, M. R. V. Lanza and A. J. Motheo, *Electrochim. Acta*, 2014, **143**, 180–187.
26 P. Finkbeiner, M. Franke, F. Anschuetz, A. Ignaszak, M. Stelter and P. Braeutigam, *Chem. Eng. J.*, 2015, **273**, 214–222.
27 J. R. Steter, M. H. Kossuga and A. J. Motheo, *Ultrason. Sonochem.*, 2016, **28**, 21–30.
28 M. Dietrich, M. Franke, M. Stelter and P. Braeutigam, *Ultrason. Sonochem.*, 2017, **39**, 741–749.
29 S. Ben Kacem, S. C. Elaoud, A. M. Asensio, M. Panizza and D. Clematis, *J. Electroanal. Chem.*, 2021, **889**, 115212.
30 M. Shestakova, M. Vinatoru, T. J. Mason, E. Iakovleva and M. Sillanpää, *J. Mol. Liq.*, 2016, **223**, 388–394.
31 R. Patidar and V. C. Srivastava, *Chemosphere*, 2020, **257**, 127121.
32 R. Patidar and V. C. Srivastava, *J. Hazard. Mater.*, 2022, **422**, 126842.
33 Y. Z. Ren, M. Franke, F. Anschuetz, B. Ondruschka, A. Ignaszak and P. Braeutigam, in *Ultrasonics Sonochemistry*, Elsevier B.V., 2014, vol. 21, pp. 2020–2025.
34 C. Yin, T. Ye, Y. Yu, W. Li and Q. Ren, *Microchem. J.*, 2019, **144**, 369–376.
35 G. Nie, Y. Yao, X. Duan, L. Xiao and S. Wang, *Curr. Opin. Chem. Eng.*, 2021, **33**, 100693.
36 M. B. Starr and X. Wang, *Nano Energy*, 2014, **14**, 296–311.
37 W. Kang, Z. Zheng, Y. Li and R. Zhao, *J. Mater. Sci.: Mater. Electron.*, 2019, **30**, 16244–16250.
38 K. S. Hong, H. Xu, H. Konishi and X. Li, *J. Phys. Chem. Lett.*, 2010, **1**, 997–1002.
39 R. Zhu, Y. Xu, Q. Bai, Z. Wang, X. Guo and H. Kimura, *Chem. Phys. Lett.*, 2018, **702**, 26–31.
40 M. Hamlehdar, A. Kasaeian and M. R. Safaei, *Renewable Energy*, 2019, **143**, 1826–1838.
41 D. J. Shin, J. H. Ji, J. Kim, G. H. Jo, S. J. Jeong and J. H. Koh, *J. Alloys Compd.*, 2019, **802**, 562–572.
42 K. M. Sangwan, N. Ahlawat, S. Rani, S. Rani and R. S. Kundu, *Ceram. Int.*, 2018, **44**, 10315–10321.
43 Z. Liang, C. F. Yan, S. Rtimi and J. Bandara, *Appl. Catal., B*, 2019, **241**, 256–269.
44 J. M. Wu, Y. G. Sun, W. E. Chang and J. T. Lee, *Nano Energy*, 2018, **46**, 372–382.
45 J. Wu, Q. Xu, E. Lin, B. Yuan, N. Qin, S. K. Thatikonda and D. Bao, *ACS Appl. Mater. Interfaces*, 2018, **10**, 17842–17849.
46 Z. Kang, N. Qin, E. Lin, J. Wu, B. Yuan and D. Bao, *J. Cleaner Prod.*, 2020, **261**, 121125.
47 M. Sharma and R. Vaish, *Mater. Today Commun.*, 2020, **25**, 101592.
48 M. Zhu, S. Li, H. Zhang, J. Gao, K. W. Kwok, Y. Jia, L. B. Kong, W. Zhou and B. Peng, *Nano Energy*, 2021, **89**, 106474.

49 D. J. Shin, D. H. Lim, B. K. Koo, M. S. Kim, I. S. Kim and S. J. Jeong, *J. Alloys Compd.*, 2020, **831**, 154792.
50 A. Bootchanont, J. Jutimoosik, S. Chandarak, M. Unruan, S. Rujirawat, R. Yimnirun, R. Guo and A. Bhalla, *Ceram. Int.*, 2013, **39**, 579–582.
51 T. Samma, T. Fuchigami, S. Nakamura, T. Fey and K. ichi Kakimoto, *Phys. Status Solidi B*, 2022, **259**, 2100611.
52 B. O. Ojo, O. A. Arotiba and N. Mabuba, *J. Environ. Chem. Eng.*, 2022, **10**, 107224.
53 S. Patel, K. S. Srikanth, S. Steiner, R. Vaish and T. Frömling, *Ceram. Int.*, 2018, **44**, 21976–21981.
54 L. Mi, Q. Zhang, H. Wang, Z. Wu, Y. Guo, Y. Li, X. Xiong, K. Liu, W. Fu, Y. Ma, B. Z. Wang and X. W. Qi, *Ceram. Int.*, 2020, **46**, 10619–10633.
55 H. Aminirastabi, H. Xue, V. V. Mitić, G. Lazović, G. Ji and D. Peng, *Mater. Chem. Phys.*, 2019, **239**, 122261.
56 S. Wirunchit, T. Charoonsuk and N. Vittayakorn, *RSC Adv.*, 2015, **5**, 38061–38074.
57 M. Sharma, G. Singh and R. Vaish, *J. Am. Ceram. Soc.*, 2020, **103**, 4774–4784.
58 A. Rached, M. A. Wederni, A. Belkahla, J. Dhahri, K. Khirouni, S. Alaya and R. J. Martín-Palma, *Phys. B*, 2020, **596**, 412343.
59 F. J. Del Campo, B. A. Coles, F. Marken, R. G. Compton and E. Cordemans, *Ultrason. Sonochem.*, 1999, **6**, 189–197.
60 S. Dahbi, N. Tahiri, O. El Bounagui and H. Ez-Zahraouy, *Chem. Phys.*, 2021, **544**, 111105.
61 R. P. Patil, P. V. More, G. H. Jain, P. K. Khanna and V. B. Gaikwad, *Vacuum*, 2017, **146**, 455–461.
62 J. R. Steter, W. R. P. Barros, M. R. V. Lanza and A. J. Motheo, *Chemosphere*, 2014, **117**, 200–207.
63 J. González-García, M. D. Esclapez, P. Bonete, Y. V. Hernández, L. G. Garretón and V. Sáez, *Ultrasonics*, 2010, **50**, 318–322.
64 J. Klima, *Ultrasonics*, 2011, **51**, 202–209.
65 B. G. Pollet, *Ultrason. Sonochem.*, 2019, **52**, 6–12.
66 N. Tran, P. Drogui and S. K. Brar, *Environ. Chem. Lett.*, 2015, **13**, 251–268.
67 F. Marken, R. P. Akkermans and R. G. Compton, *J. Electroanal. Chem.*, 1996, **415**, 55–63.
68 Z. Liang, C. F. Yan, S. Rtimi and J. Bandara, *Appl. Catal., B*, 2019, **241**, 256–269.
69 B. O. Ojo, O. A. Arotiba, N. Mabuba and N. Sciences, *Colloids Surf., A*, 2022, **647**, 129201.
70 K. Kim, E. Cho, B. Thokchom, M. Cui, M. Jang and J. Khim, *Ultrason. Sonochem.*, 2015, **24**, 172–177.
71 J. Ma, J. Ren, Y. Jia, Z. Wu, L. Chen, N. O. Haugen, H. Huang and Y. Liu, *Nano Energy*, 2019, **62**, 376–383.
72 K. Govindan, D. G. Kim and S. O. Ko, *J. Environ. Chem. Eng.*, 2022, **10**, 108257.
73 P. Raja, A. Bozzi, H. Mansilla and J. Kiwi, *J. Photochem. Photobiol., A*, 2005, **169**, 271–278.
74 G. Xiao, T. Xu, M. Faheem, Y. Xi, T. Zhou, H. T. Moryani, J. Bao and J. Du, *Int. J. Environ. Res. Public Health*, 2021, **18**, 3344.
75 M. H. Islam, O. S. Burheim and B. G. Pollet, *Ultrason. Sonochem.*, 2019, **51**, 533–555.
76 S. Dzwigaj and H. Pezerat, *Free Radic. Res.*, 2009, **23**, 103–115.
77 C. Su, R. Li, C. Li and W. Wang, *Appl. Catal., B*, 2022, **310**, 121330.
78 J. Ayarza, Z. Wang, J. Wang, C. W. Huang and A. P. Esser-Kahn, *ACS Macro Lett.*, 2020, **9**, 1237–1248.
79 D. Seibert, C. F. Zorzo, F. H. Borba, R. M. de Souza, H. B. Quesada, R. Bergamasco, A. T. Baptista and J. J. Inticher, *Sci. Total Environ.*, 2020, **748**, 141527.
80 T. Tang, M. Liu, Y. Chen, Y. Du, J. Feng and H. Feng, *J. Hazard. Mater.*, 2022, **431**, 128540.
81 S. Sheikhi, B. Jebalbarezi, R. Dehghanzadeh, A. Maryamabadi and H. Aslani, *J. Environ. Chem. Eng.*, 2022, **10**, 107446.
82 Y. Huang, T. Zhou, X. Wu and J. Mao, *Ultrason. Sonochem.*, 2017, **38**, 735–743.
83 J. He, J. Huang, Z. Wang, Z. Liu, Y. Chen, R. Su, X. Ni, Y. Li, X. Xu, W. Zhou, B. Gao and Q. Li, *Chem. Eng. J.*, 2022, **439**, 135784.